

Look at Adjacent Frames: Video Anomaly Detection without Offline Training

Yuqi Ouyang, Guodong Shen, and Victor Sanchez

University of Warwick

{yuqi.ouyang, guodong.shen, v.f.sanchez-silva}@warwick.ac.uk

Abstract. We propose a solution to detect anomalous events in videos without the need to train a model offline. Specifically, our solution is based on a randomly-initialized multilayer perceptron that is optimized online to reconstruct video frames, pixel-by-pixel, from their frequency information. Based on the information shifts between adjacent frames, an incremental learner is used to update parameters of the multilayer perceptron after observing each frame, thus allowing to detect anomalous events along the video stream. Traditional solutions that require no offline training are limited to operating on videos with only a few abnormal frames. Our solution breaks this limit and achieves strong performance on benchmark datasets.

Keywords: Video Anomaly Detection, Unsupervised, Offline Training, Online Learning, Multilayer Perceptron, Discrete Wavelet Transform

1 Introduction

Video anomaly detection (VAD) aims at detecting anomalous events in a video scene. Since it is hard to define all possible anomalous events a priori and moreover, these anomalies may occur infrequently, VAD is rarely solved by supervised learning. It is then common to exclusively rely on normal video data to train a model for the detection of anomalous events. Hence, the lack of examples of abnormal events during training defines the inherent challenges of this task. However, real-life experiences show that a person could react to a biker moving among pedestrians because the biker moves distinctively, without knowing that the biker is an abnormality in this context. Enlightened by such human intelligence, VAD can also be solved without any knowledge learned from an offline training process by analyzing spatio-temporal differences between adjacent frames since these differences are usually significant where anomalous events occur [10,15,20]. The working mechanism of this type of VAD solution, which requires no offline training and is hereinafter referred to as online VAD¹ is illustrated in Fig. 1 along with the working mechanism of offline VAD. Note that instead of training the model offline, online VAD updates the model sequentially after observing each video frame, thus requiring no training data.

¹ Note that in this paper, online VAD does not refer to VAD solutions that are trained offline but operate at high frame rates.

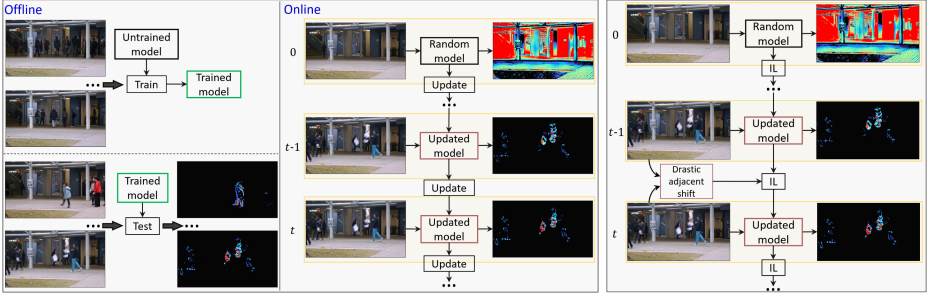


Fig. 1: Working mechanisms of offline and online VAD. Fig. 2: Idea of online VAD.

One main advantage of online VAD is that a model can learn beyond the data used for offline training and adapt much better to the data source during operation, which eases the issue of concept drift caused by, e.g., any data distribution difference between the offline and online data. In offline VAD, a model is trained first to understand the patterns of videos depicting normal events. Once trained, it is used on new videos depicting normal events and possibly, abnormal events. In this case, the concept drift due to the distribution differences between the offline and online data depicting normal events may result in poor performance during operation. To deal with such a concept drift, one can use human support to regularly identify those normal frames on which the model performs poorly, and then retrain the model to recognize these frames correctly. However, such an approach undoubtedly comes with an extra workload.

Despite the fact that the performance of VAD solutions has improved recently [9,35], online VAD solutions are still scarce [28,36]. Moreover, the existing ones are usually flawed. For example, [10,15,20], which are pioneers in online VAD, attain poor performance on videos with a large number of anomalous events. Motivated by these limitations, we present our idea for online VAD in Fig. 2. Our idea focuses on the spatio-temporal differences between adjacent frames, hereinafter referred to as adjacent shifts. It uses an incremental learner (IL) that accounts for the adjacent shifts and sequentially updates the model from a set of randomly-initialized parameters. The IL is expected to easily adapt to gradual adjacent shifts, which usually exist between normal frames and should result in no anomaly detections. Conversely, the IL is expected to encounter difficulties in adapting to drastic adjacent shifts, which usually exist between abnormal frames or between a normal and an abnormal frame, thus resulting in anomaly detections. More specifically, as illustrated in Fig. 3, our solution generates error maps as the detection results by reconstructing spatio-temporal information and pixel coordinates into pixel values and comparing the reconstructed frames with the original ones. In this work, we use the discrete wavelet transform (DWT) to summarize the spatio-temporal information of a video sequence and a Multi-layer Perceptron (MLP) for the frame reconstruction task. The MLP is set to be updated by the IL while adapting to the adjacent shifts, after observing each frame. The contributions of this work are summarized as follows:

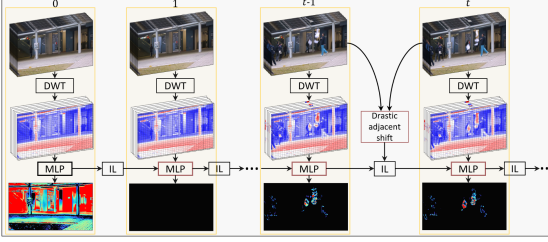


Fig. 3: Our solution to online VAD.

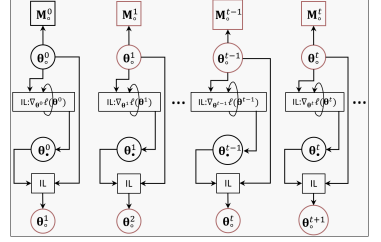


Fig. 4: Our problem definition.

- We introduce the first MLP-based model that uses frequency information to produce pixel-level VAD results.
- More importantly, we design a novel solution for online VAD, i.e., detecting anomalous events with **no** offline training, where the network parameters are optimized sequentially after observing each frame starting from random initialization.
- We achieve state-of-the-art performance on benchmark datasets regardless of the temporal order or the number of abnormal frames in a video.

2 Related Work

Offline VAD. State-of-the-art offline VAD solutions use deep-learning techniques. These models can be classified as unsupervised, weakly-supervised, or self-supervised depending on the training data and how these data are used. Unsupervised models exclusively employ normal videos for training, with data mapping via an encoder-decoder structure being the most frequently used strategy. The baseline approaches in this context are based on data reconstruction or prediction, where anomalous events are detected based on the reconstruction or prediction errors, respectively [12,52,24,29,49,21,38]. Adversarial losses can also be applied in such approaches, where the generator is adversarially trained to perform the data mapping so that abnormal videos lead to unrealistic outputs with large reconstruction or prediction errors [37,19,45,30,51]. If the features extracted from the normal and abnormal videos form two distinct and compact clusters, anomalous events can be detected in a latent subspace. In this type of approach, two ways are usually used to train a model. Either separately training the feature extraction and clustering steps [48,13,14,41,32], or jointly training both steps end-to-end [1,11,34,3,27,2].

Weakly-supervised models use a small number of abnormal frames with labels for training. Based on the triplet loss [18] or multiple instance learning strategy [40,54,53,7,44,35], such models can learn to increase the inter-class distance between normal and abnormal data. Weakly-supervised models outperform unsupervised models but they require abnormal data with ground truth labels [50,7,44].

Self-supervised models are becoming increasingly popular [46,33]. These models are trained with both normal and abnormal videos but without ground truth labels. They are usually trained iteratively by simulating labels through decision-making and then optimizing parameters based on the simulated labels. Data collection is easier for these models because they do not require ground truth labels. However, because these models may use some of the test videos in the training stage, their results should be interpreted with caution.

Online VAD. Compared to offline VAD solutions, online models are limited both in numbers and performances [28,36]. Three main models [10,15,20] have been designed to tackle VAD online. The seminal work in [10] detects anomalous events by aggregating anomaly values from several frame shuffles, where the anomaly value in each shuffle is calculated by measuring the similarity between all previous frames and the frames in a sliding window. Although that particular model cannot work with video streams, it sets an important precedent for VAD online. The follow-up works in [15,20] propose analyzing adjacent frame batches, where anomalies are defined as abrupt differences in spatio-temporal features between two adjacent batches. However, instead of randomly initializing a model and continuously optimizing it along the video stream, these two works repeat the random initialization of parameters every time a new frame is observed, ignoring the fact that frames may share common information, such as the scene background. Moreover, the performances of these three solutions, i.e., [10,15,20], degrades when used on videos with a large number of anomalous events.² The reason for this is that those models assume a video only contains a few abnormal frames, thus a large number of abnormal frames violate their assumptions regarding the spatio-temporal distinctiveness of abnormal frames in a video.

Offline VAD with further optimization. Recently, several offline VAD solutions that are further optimized online have been proposed [4,5,6]. Specifically, these models are first trained offline and then refined online to reduce false positives. Namely, the model processes each frame online and adds potential normal frames to a learning set where false positives identified manually are also included [4]. Such a learning set is then used to further optimize the model so that it can more accurately learn the normal patterns beyond the offline training data. Scene adaptation has also been recently addressed in VAD [23,25] based on recent advance in meta-learning [8]. Specifically, the model is first trained offline to produce acceptable results for a variety of scenes, and is then further optimized with only a few frames from a specific scene of interest, thus rapidly adapting to that scene.

3 Proposed Solution

Problem definition. Based on our objective of generating pixel-level detections online in the form of error maps, we start by providing the problem definition:

² Videos with more than 50% of frames being abnormal.

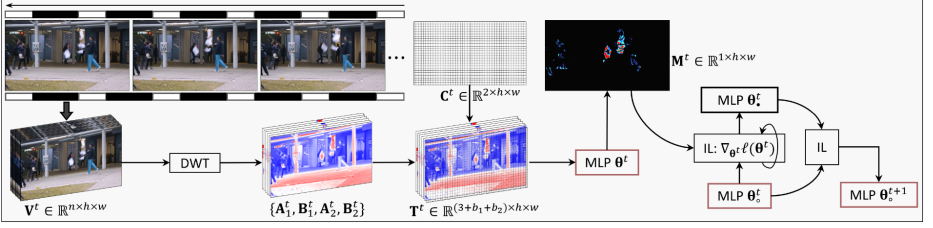


Fig. 5: The workflow of our solution at timestep t . b_1 and b_2 respectively indicate the number of high-frequency maps in tensors \mathbf{B}_1^t and \mathbf{B}_2^t of the temporal DWT.

- At current timestep t , based on the network parameters θ_0^t , compute the error map \mathbf{M}^t , where anomalies are indicated at the pixel-level.
- Define the loss $\ell(\theta^t)$ to optimize θ_0^t into θ_{\bullet}^t .
- Use θ_0^t and θ_{\bullet}^t to define θ_0^{t+1} for computing an error map for timestep $t+1$.

Note that we use two types of subscripts, i.e., a clear circle \circ and a black circle \bullet , where \circ (\bullet) denotes the initial (final) network parameters or the detection results before (after) the optimization process. We illustrate our problem definition in Fig. 4 starting from the first frame of a video stream, i.e., $t=0$, where the IL is in charge of updating the network parameters from θ_0^t to θ_{\bullet}^t and subsequently computing θ_0^{t+1} .

3.1 Workflow

Fig. 5 illustrates the workflow of our solution at the current timestep t .³ It first applies a temporal DWT to a set of n frames of size $h \times w$ where the last frame is the current frame \mathbf{I}^t , denoted by \mathbf{V}^t , to generate DWT coefficients. The DWT coefficients are used in conjunction with the pixel coordinates \mathbf{C}^t as the input \mathbf{T}^t of a pixel-level MLP to reconstruct \mathbf{I}^t , thus leading to an error map \mathbf{M}^t by comparing the reconstruction results with the ground truth frame. \mathbf{M}^t is then used by the IL to define the loss $\ell(\theta^t)$. Based on $\ell(\theta^t)$, the IL updates the network parameters from θ_0^t to θ_{\bullet}^t , and then calculates θ_0^{t+1} for the next timestep.

Discrete wavelet transform. In this work, we use the temporal DWT to summarize the spatio-temporal information of a video sequence because it has been shown to provide motion information that fits the human visual system [16]. As shown in Fig. 6 (left), two levels of temporal DWT are performed on the set of frames \mathbf{V}^t . The temporal DWT results in four tensors of sub-bands. Specifically, two low-frequency tensors, \mathbf{A}_1^t and \mathbf{A}_2^t , and two high-frequency tensors, \mathbf{B}_1^t and \mathbf{B}_2^t . Note that the temporal DWT does not change the spatial dimensions. The input tensor \mathbf{T}^t of our MLP is defined as:

$$\mathbf{T}^t = [\mathbf{C}^t, \mathbf{A}^t, \mathbf{B}_1^t, \mathbf{B}_2^t], \quad (1)$$

³ In Figs. 5 and 6, the channel dimensions of the data is omitted

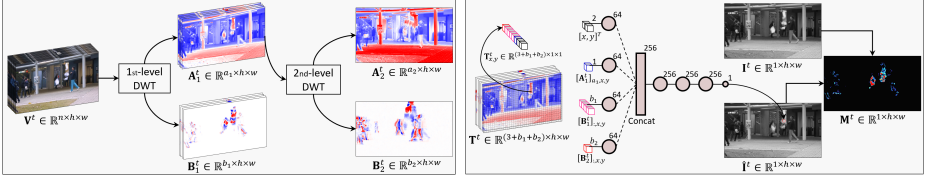


Fig. 6: Details of our temporal DWT (left) and our MLP (right). a_1 and a_2 (b_1 and b_2) respectively indicate numbers of low-frequency (high-frequency) maps in tensors A_1^t and A_2^t (B_1^t and B_2^t) of the temporal DWT. Layers of the MLP are depicted with the dimensions of their outputs. The error map is computed by comparing two grayscale images.

where $A^t \in \mathbb{R}^{1 \times h \times w}$ is the last low-frequency map of the tensor A_1^t . Here T^t is formed by stacking the coordinate tensor C^t , the low-frequency map A^t (appearance information), the first-level high-frequency tensor B_1^t (sparse motion information) and the second-level high-frequency tensor B_2^t (dense motion information) along the first dimension.

Multilayer perceptron. We use an MLP to reconstruct frames because it has been shown to effectively map pixel coordinates into pixel values [39, 43, 42]. As illustrated in Fig. 6 (right), our MLP maps T^t into the reconstructed frame \hat{I}^t . Given such an MLP with parameters θ^t , the resulting error map, M^t , and its mean squared error (MSE), ϵ^t , are respectively computed as follows:

$$M^t = (I^t - f_{\theta^t}(T^t))^{\odot 2}, \quad (2)$$

$$\epsilon^t = \frac{1}{hw} \|M^t\|_1, \quad (3)$$

where $f_{\theta^t}(\cdot)$ denotes the mapping function of the MLP, \odot^2 indicates element-wise square, and $\|\cdot\|_1$ indicates ℓ_1 -norm.⁴ The MLP is optimized by an IL, as detailed next.

3.2 Incremental Learner

As illustrated in Fig. 7 (left), at the current timestep t , the IL comprises a comparator that defined the loss $\ell(\theta^t)$ from MLP results, an adapter that optimizes the parameters of the MLP based on $\ell(\theta^t)$, and a clipper that calculates the initial parameters of the MLP for the next timestep, i.e., θ_o^{t+1} .

The comparator. This component compares the reconstruction results of frame I^{t-1} , as reconstructed by the MLP with parameters θ_o^{t-1} , with those of frame I^t , as reconstructed by the MLP with parameters θ^t . Based on this comparison,

⁴ To compute the error map and the MSE when optimizing the MLP, please follow Eqs. (2) and (3) but replace θ^t with current parameter set involved in the optimization; e.g., $M_o^t = (I^t - f_{\theta_o^t}(T^t))^{\odot 2}$, $\epsilon_o^t = \frac{1}{hw} \|M_o^t\|_1$.

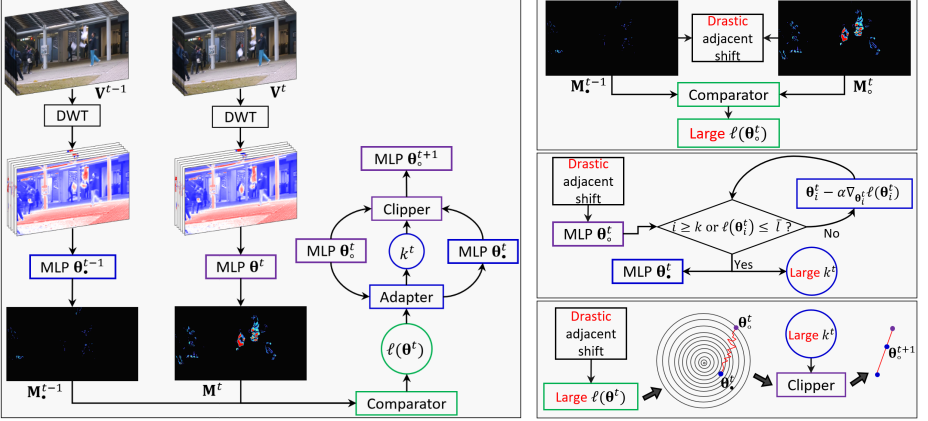


Fig. 7: The incremental learner at the current timestep t (left). An example of a drastic adjacent shift that results in a large value for the loss function (top-right). The iterative process used to update the parameters of the MLP (middle-right). Computation of the initial parameters of the MLP for timestep $t + 1$ (bottom-right).

it defines the loss $\ell(\theta^t)$ for the MLP at timestep t . This loss is based on MSE values:

$$\ell(\theta^t) = \text{Relu}(\epsilon^t - \epsilon_{\bullet}^{t-1}), \quad \text{if } t \geq 1. \quad (4)$$

The rationale behind the loss in Eq. (4) is that such comparison accounts for the adjacent shift between frames I^{t-1} and I^t . Fig. 7 (top-right) shows an example, where a drastic adjacent shift causes that a well-fitted MLP (θ_{\bullet}^{t-1}) accurately reconstructs frame I^{t-1} but the precedent MLP (θ_o^{t-1}) poorly reconstructs frame I^t , thus such a comparison implicitly measures the adjacent shift by resulting in a large loss $\ell(\theta^t)$ at the beginning, i.e., $\ell(\theta_{\bullet}^t)$.⁵

For the first frame of a video sequence, i.e., timestep $t = 0$, note that there is no previous information for the comparator to define the loss in Eq. (4). We say that, in this case, the randomly-initialized MLP is under a cold start and may not generate accurate reconstruction results. Hence, we adjust Eq. (4) for $t = 0$ as follows:

$$\ell(\theta^t) = \text{Relu}(\epsilon^t - \bar{\epsilon}), \quad \text{if } t = 0, \quad (5)$$

where $\bar{\epsilon}$ is a user-defined MSE value that defines a target value to be achieved for an accurate reconstruction.⁶

The adapter. Based on the loss $\ell(\theta^t)$, the adapter adapts to the adjacent shift by optimizing the parameters of the MLP at each timestep over several iterations of gradient descent (GD), the $(i + 1)_{\text{th}}$ GD iteration is defined as:

$$\theta_i^t \xrightarrow{-\nabla_{\theta_i^t} \ell(\theta_i^t), \text{ if } \ell(\theta_i^t) > \bar{\ell} \text{ or } i < \bar{k}} \theta_{i+1}^t, \quad (6)$$

⁵ To compute the loss when optimizing the MLP, please follow Eq. (4) or Eq. (5) but replace θ^t with current parameter set involved in the optimization; e.g., $\ell(\theta_o^t) = \text{Relu}(\epsilon_o^t - \epsilon_{\bullet}^{t-1})$, (if $t \geq 1$).

⁶ We set $\epsilon_{\bullet}^{t-1} = \max(\epsilon_{\bullet}^{t-1}, \bar{\epsilon})$ in Eq. (4) to prevent our MLP being overfitted towards a MSE value lower than the lower-bound $\bar{\epsilon}$.

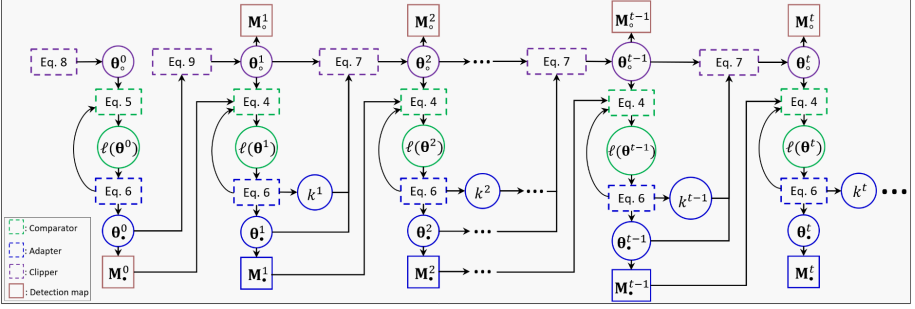


Fig. 8: The mathematical operations of the IL along a video stream.

where $i \in [0, \bar{k}]$. Here we use two user-defined parameters, i.e., \bar{k} and \bar{l} , to control the end of the iterative optimization: the adapter stops at the current GD iteration if the number of GD iterations is large enough ($i \geq \bar{k}$) or if the loss is small enough ($\ell(\theta_o^i) \leq \bar{l}$). This iterative process is illustrated in Fig. 7 (middle-right), where the adapter optimizes the parameters from θ_o^t to θ_o^t .⁷

Let k^t denote the number of iterations of GD used by the adapter at timestep t . A large loss $\ell(\theta_o^t)$, potentially caused by the drastic adjacent shift, will cause the adapter spend many iterations of GD, i.e., a large k^t , to optimize network parameters.

The clipper. According to Fig. 7 (left), the loss $\ell(\theta_o^{t+1})$ at the next timestep $t+1$, should be computed by comparing \mathbf{M}_o^t , as computed under the parameter set θ_o^t , and \mathbf{M}_o^{t+1} , as computed under the parameter set θ_o^{t+1} . Since the adapter generates θ_o^t , we need to define the initial parameter set θ_o^{t+1} . This is accomplished by the clipper.

Illustrated in Fig. 7 (middle-right), a large value of k^t , i.e., the number of iterations of GD used by the adapter at timestep t , may imply a drastic shift between frames \mathbf{I}^{t-1} and \mathbf{I}^t . Such a drastic shift may indicate that the current frame \mathbf{I}^t is abnormal. Hence, the MLP may have been well-fitted to reconstruct the abnormal frame \mathbf{I}^t , and such a well-fitted parameter set θ_o^t may not be appropriate for use to initialize θ_o^{t+1} . Based on these observations, θ_o^{t+1} is defined based on knowledge transfer [31] by clipping between θ_o^t and θ_o^t as follows:

$$\theta_o^{t+1} = \theta_o^t + (k^t)^{-\frac{1}{2}} (\theta_o^t - \theta_o^t), \quad \text{if } t \geq 1. \quad (7)$$

For a large k^t , potentially caused by the drastic adjacent shift, θ_o^{t+1} is set close to θ_o^t , thus rejecting the learned knowledge θ_o^t acquired from a potential abnormal frame \mathbf{I}^t . This is illustrated in Fig. 7 (bottom-right).

Since there is no previously learned knowledge at $t=0$, the MLP is randomly-initialized for this first frame as:

$$\theta_o^0 = \tilde{\theta}, \quad (8)$$

⁷ Note that $\theta_o^t = \theta_o^t$.

Algorithm 1 The IL

```

1:  $i \leftarrow 0$ 
2:  $\theta_{\circ}^t \leftarrow \theta_{\circ}^t$ 
3: while True do
4:    $\mathbf{M}_i^t \leftarrow (\mathbf{I}^t - f_{\theta^t}(\mathbf{T}^t))^{\odot 2}$ 
5:    $\epsilon_i^t \leftarrow \frac{1}{hw} \|\mathbf{M}_i^t\|_1$ 
6:    $\mathbf{M}_{\circ}^t \leftarrow \mathbf{M}_{\circ}^t$ ,  $\epsilon_{\circ}^t \leftarrow \epsilon_{\circ}^t$  when  $i = 0$ 
7:    $\ell(\theta_i^t) \leftarrow \text{COMPARE}(\bar{\epsilon}, \epsilon_{\bullet}^{t-1}, \epsilon_i^t)$ 
8:   if  $\ell(\theta_i^t) \leq \bar{\ell}$  or  $i \geq \bar{k}$  then
9:     break
10:  else
11:     $\theta_{i+1}^t \leftarrow \text{ADAPT}(\alpha, \nabla_{\theta^t} \ell(\theta_i^t))$ 
12:     $i \leftarrow i + 1$ 
13:   $\theta_{\bullet}^t \leftarrow \theta_{\bullet}^t$ ,  $\mathbf{M}_{\bullet}^t \leftarrow \mathbf{M}_{\bullet}^t$ ,  $\epsilon_{\bullet}^t \leftarrow \epsilon_{\bullet}^t$ 
14:   $\theta_{\circ}^{t+1} \leftarrow \text{CLIP}(\theta_{\circ}^t, \theta_{\bullet}^t, k^{t-1})$ 
15:   $k^t \leftarrow (\text{if } i = 0 \text{ then } 1 \text{ else } i \text{ end})$ 
16:   $\mathbf{M}_{\text{det}}^t \leftarrow (\text{if } t = 0 \text{ then } \mathbf{M}_{\bullet}^t \text{ else } \mathbf{M}_{\circ}^t \text{ end})$ 
17:  $\mathcal{RETUR}\mathcal{N}(\theta_{\circ}^{t+1}, \epsilon_{\bullet}^t, k^t, \mathbf{M}_{\text{det}}^t)$ 

```

Algorithm 2 Compute detection maps

```

1:  $\mathbb{M}_{\text{det}} \leftarrow \emptyset$ 
2:  $t \leftarrow 0$ 
3:  $\theta_{\circ}^0 \leftarrow \mathcal{RAND}()$ 
4:  $\epsilon_{\bullet}^{-1} \leftarrow \text{null}$ 
5:  $k^{-1} \leftarrow \text{null}$ 
6: while True do
7:   if  $\mathbf{V}^t$  not exists then
8:     break
9:    $\mathbf{V}^t \leftarrow \text{TRANSFORM}(\mathbf{V}^t)$ 
10:   $\mathbf{C}^t \leftarrow \text{TRANSFORM}(\mathbf{C}^t)$ 
11:   $\mathbf{A}_1^t, \mathbf{B}_1^t, \mathbf{A}_2^t, \mathbf{B}_2^t \leftarrow \text{DWT}(\mathbf{V}^t)$ 
12:   $\mathbf{T}^t \leftarrow [\mathbf{C}^t, [\mathbf{A}_1^t]_{a_1, :, :}, \mathbf{B}_1^t, \mathbf{B}_2^t]$ 
13:   $\theta_{\bullet}^{t+1}, \epsilon_{\bullet}^t, k^t, \mathbf{M}_{\text{det}}^t \leftarrow \mathcal{IL}(\mathbf{I}^t, \mathbf{T}^t, \theta_{\circ}^t, \epsilon_{\bullet}^{t-1}, k^{t-1})$ 
14:   $\mathbb{M}_{\text{det}} \leftarrow \mathbb{M}_{\text{det}} \cup \{\mathbf{M}_{\text{det}}^t\}$ 
15:   $t \leftarrow t + 1$ 

```

where $\tilde{\theta}$ indicates a random set of parameters. At $t=1$, the MLP is initialized without clipping parameters to avoid using the randomly-initialized parameters θ_{\circ}^0 as:

$$\theta_{\circ}^1 = \theta_{\bullet}^0. \quad (9)$$

Fig. 8 illustrates the complete functionality of the IL along a video stream, while Alg. 1 summarizes it.

Detection and anomaly inference. As depicted in Fig. 8, at the current timestep t , the MLP with initial parameters θ_{\circ}^t results in an error map \mathbf{M}_{\circ}^t as the detection results, hereinafter called detection maps. For all observed frames, these detection maps are:

$$\mathbb{M}_{\text{det}} = \{\mathbf{M}_{\bullet}^0, \mathbf{M}_{\circ}^1, \mathbf{M}_{\circ}^2, \dots, \mathbf{M}_{\circ}^t\}, \quad (10)$$

where at $t=0$, we use the detection map \mathbf{M}_{\bullet}^0 computed after the optimization.⁸ The detection maps can be visually displayed as heatmaps that depict the abnormal pixels,⁹ or alternately, one can calculate the MSE values associated with these maps to numerically quantify the anomalies. Alg. 2 summarizes the process to compute the detection maps.

4 Experiments

Datasets. We test our model on three benchmark datasets. The UCSD Ped2 [26] dataset, which is a single-scene dataset depicting a pedestrian walkway where the anomalous events are individuals cycling, driving or skateboarding. The CUHK Avenue [22] dataset, which is also a single-scene dataset depicting a subway entrance with various types of anomalous events, such as individuals throwing

⁸ Since \mathbf{M}_{\circ}^0 is a noisy error map generated by the MLP under random-initialization.

⁹ See examples of detection maps in Fig. 11.

papers and dancing. And the ShanghaiTech [24] dataset, which is more difficult to analyze as it has complex anomalous events across multiple scenes.¹⁰

Non-continuous videos. In each benchmark dataset, videos depicting the same scene may not be continuously shot by one camera. Hence, our model regards these videos as different video streams. However, since such video streams may share common information, e.g., the background information, instead of randomly initializing our model on the first frame of these video streams, as specified in Eq. (8), our model initializes the parameters by transferring the knowledge learned on the last frame of the previous video stream. Note that for continuous videos depicting the same scene and shot by one camera, our model computes the initial parameters as specified by Fig. 8.

Implementation details. All frames are transformed into gray-scale images and respectively re-sized to 230×410 and 240×428 for the CUHK Avenue and ShanghaiTech datasets. All pixel coordinates and pixel values are re-scaled to the range $[-0.5, 0.5]$. *Daubechies 2* is used as the filter for the temporal DWT on each set of video frames \mathbf{V}^t of length $n = 16$. We randomly initialize the parameters of our MLP based on the settings provided in [39].¹¹ Adam [17] is used with learning rates 1×10^{-4} and 1×10^{-5} , respectively, on the first frame and subsequent frames of all videos. The two user-defined parameters, $\bar{\epsilon}$ and \bar{l} , are respectively set to 1×10^{-4} and 1×10^{-6} on all videos. \bar{k} is set to 500 on the first 5 frames of each video, and then to 100 on the remaining frames.

Evaluation metrics. We use the frame-level Area Under the Curve (AUC) of the Receiver Operating Characteristic (ROC) curve as the evaluation metric. Higher AUC values indicate better model performance.

4.1 Performance

In Tab. 1, we tabulate the performances of our model and other baseline models, where we highlight the best performing model in **bold** and underline the second best performing model. The left part of Tab. 1 tabulates the performances of online VAD solutions, while the right part compares ours with offline VAD solutions. Note that since the other three online VAD solutions cannot work on videos with a large number of abnormal frames while our model does not have that restriction, substantially more videos are tested by our solution. Despite more videos being analyzed, our model outperforms the best model previously reported in [20] by 9.0% and 5.8% AUC, respectively, on the UCSD Ped2 and CUHK Avenue datasets. Note that we report the first result computed by an online VAD solution on the ShanghaiTech dataset, i.e., an AUC value of 83.1%. Compared to offline VAD solutions, the performance of our solution is very competitive, outperforming most of the models on the ShanghaiTech dataset with an AUC value of 83.1%, which confirms our robustness to deal with complex scenes. The best performing offline solution is [9], which relies on multiple tasks where several networks are separately trained offline to jointly detect anomalies.

¹⁰ The dataset has 13 scenes but there are no test videos for the last scene, thus we only focus on the first 12 scenes.

¹¹ All activation functions are *Sine* and only the last layer has no activation function.

Table 1: Comparisons in frame-level AUC values (%) on three benchmark datasets with online VAD models (left) and offline VAD models (right).

	Giorno	Iones-	Liu	Ours		Chang	Lu	Wang	Sun	Cai	Lv	George-	Liu	Ours
	[10]	cu [15]	[20]			[3]	[23]	[47]	[41]	[2]	[25]	scu [9]	[21]	
UCSD Ped2	-	82.2	<u>87.5</u>	96.5	UCSD Ped2	96.5	96.2	-	-	96.6	96.9	99.8	<u>99.3</u>	96.5
CUHK Avenue	78.3	80.6	<u>84.4</u>	90.2	CUHK Avenue	86.0	85.8	87.0	89.6	86.6	89.5	92.8	<u>91.1</u>	90.2
Shang-haiTech	-	-	-	83.1	Shang-haiTech	73.3	77.9	79.3	74.7	73.7	73.8	90.2	76.2	<u>83.1</u>

Our solution attains competitive results by detecting video anomalies on-the-fly without offline training under a single framework based on frame reconstruction.

4.2 Further Studies

Abnormal start. As specified in Eq. (5), our solution optimizes the MLP on the first frame of a video stream for accurate reconstruction results even if that frame may be abnormal. However, even in such a case, the detection of anomalies at subsequent abnormal frames is not affected. We illustrate this in Fig. 9, which depicts the anomaly values computed on the UCSD Ped2 test video *008* as normalized MSE values (see the blue curve). In this sequence, all frames are abnormal. Notice that even after optimizing the MLP on the first abnormal frame to achieve a low reconstruction error, which leads to an anomaly value close to 0, the anomaly values increase rather than remaining low for subsequent frames. These values eventually become quite informative to detect anomalous events. The reason for this behavior is that our solution exploits the drastic adjacent shifts that exist between abnormal frames. Hence, despite being fine-tuned on the first abnormal frame, our MLP still leads to high MSE values on subsequent abnormal frames.

Unlimited amount of anomalies. Fig. 9 also confirms that our solution works very well even on a video containing only abnormal frames, which is a major improvement from the previous online VAD solutions [10,15,20], whose performances degrade on videos with a large number of abnormal frames (i.e., more than 50% of the frames depicting anomalous events). As mentioned before, a large number of abnormal frames in a video violate their assumptions that a video only contains a few abnormal frames, i.e., the spatio-temporal distinctiveness of abnormal frames in a video. Conversely, our solution makes no such assumptions, thus being capable of working on videos containing plenty of abnormal frames, or even on videos with abnormal frames only.

Pixel-level detection. In Fig. 9, we select samples of pixel-level detection for three frames, i.e., frames 23, 33 and 179 (pinned with green circles),¹² and

¹² Index numbers in the figure are 8, 18 and 164, respectively, since our model begins analyzing this sequence at the 16_{th} frame.

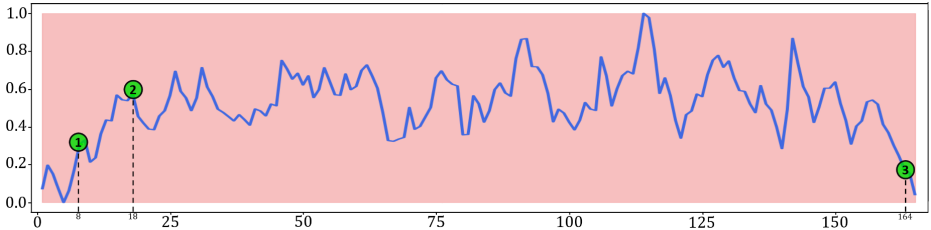


Fig. 9: Anomaly values of the UCSD Ped2 video 008, where frames 23, 33 and 179 are pinned with a green circle.

Table 2: Frame-level AUC values (%) when testing with and without the clipper.

	Ours w/o clipper	Ours
CUHK Avenue	86.3	90.2
Shang- haiTech	79.8	83.1

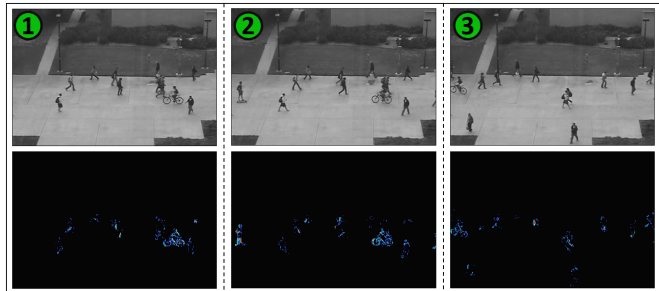


Fig. 10: Frame 23, 33 and 179 of the UCSD Ped2 video 008 and their corresponding detection maps.

illustrate these frames and their detection maps in Fig. 10. By examining these detection maps, one can see that since the cycling event is detected in all three frames, the skateboarding event should be responsible for the changes in anomaly values in Fig. 9. Specifically, its presence and disappearance, respectively, lead to an increase in the anomaly value of the second frame (frame 33) and a decrease in the third frame (frame 179). Moreover, when the skateboarder gradually enters (leaves) the scene, our solution detects it with an increasing (decreasing) trend on anomaly values (see the blue curve before frame 33, and before frame 179 in Fig. 9), which shows that our solution can detect anomalous events at the frame boundaries where the anomalies are usually not evident enough.

Fig. 11 shows examples of detection maps and their corresponding frames¹³. These sample results confirm the advantages of our pixel-level detections by demonstrating that our solution can identify video anomalies at a fine granularity level. For example, it can detect the umbrellas held by bikers (see the example in the last row, third column), small abnormal objects located in the background (see the examples at the sixth row, first column, and in the last row, fourth column). The visual results in Fig. 11 also show that our solution accurately reconstructs the scene background and foreground where pixel errors

¹³ We use *matplotlib rainbow* as the colormap, with its colors being replaced by black at low values to increase the contrast.

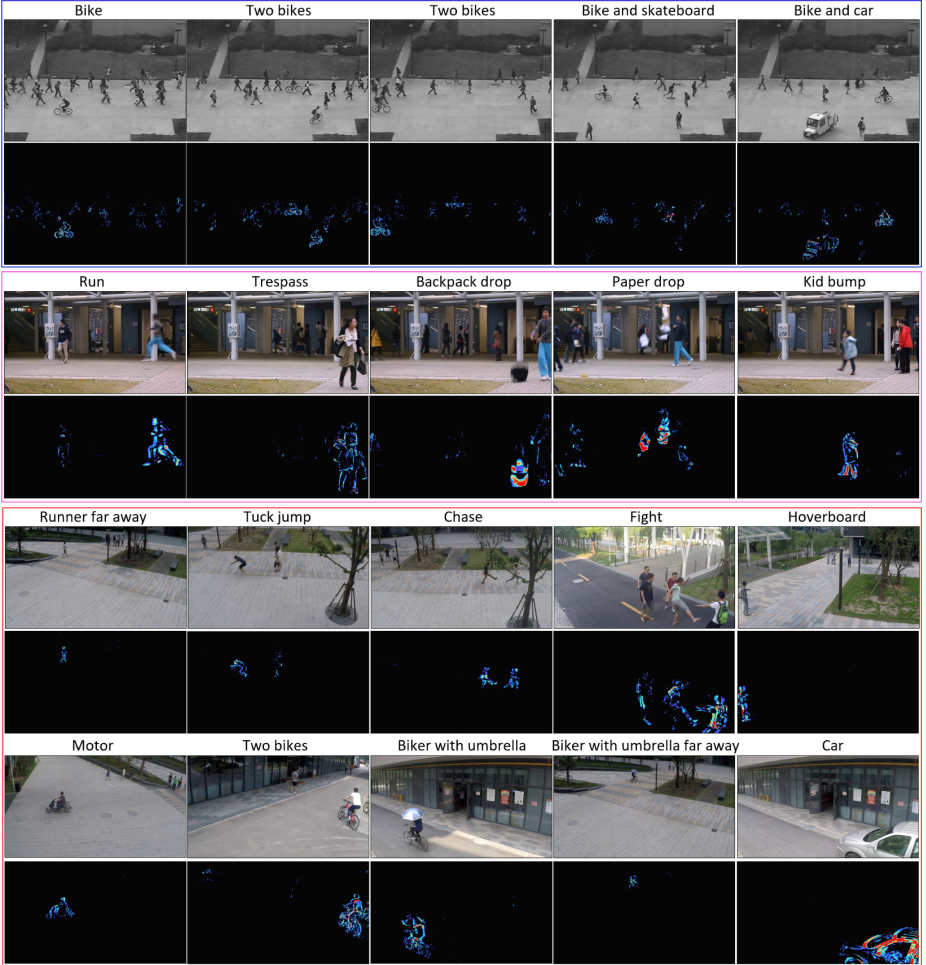


Fig. 11: Examples of frames and their detection maps of the UCSD Ped2 (rows 1-2), CUHK Avenue (rows 3-4) and ShanghaiTech (rows 5-8) datasets, where the type of anomalous event is indicated above each example. Our solution accurately detects various types of anomalous events at the pixel-level.

may be hardly recognizable. This demonstrates that the IL used by our solution successfully transfers common information along the video stream.

The clipper. We perform an ablation study to showcase the functionality of the clipper. First, we use our solution on two benchmark datasets without using the clipper, i.e., directly setting $\theta_o^t = \theta_{\bullet}^{t-1}$, and then tabulate its performance in terms of AUC values with that attained by using the clipper (see Tab. 2). These results show that by using the clipper, the performance increases, respectively, by 3.9% and 3.3% on the CUHK Avenue and ShanghaiTech datasets.



Fig. 12: Anomaly values based on normalized MSE from frames 620 to 715 of the CUHK Avenue dataset video 006 (left). Frame 625 (row 1) and 631 (row 2) and their detection maps computed without (column 2) and with (column 3) the clipper (right).

To further understand the effect of the clipper on performance, we focus on frames 620 to 715 of the CUHK Avenue test video 006, which depicts the end of an anomalous event, i.e., a person trespasses and walks out of the scene. The anomaly values computed with and without the clipper are plotted in Fig. 12 (left) in blue and red curves, respectively. Frames 625 and 631 and their detection maps are depicted in Fig. 12 (right).¹⁴ Regardless of whether the clipper is used, our solution produces informative detection maps to detect the anomalous event in frame 625 (first row). For frame 631 (second row), which is the first frame after the anomalous event ends, one can see that when the clipper is not used, our solution produces a noisier detection exactly in the region where the person leaves the scene. The pixels erroneously marked as abnormal in this error map are the results of overfitting the model on the previous abnormal frames. As depicted from the red curve in Fig. 12 (left), such overfitted model generates higher anomaly values in subsequent normal frames, which causes poorer performance. Hence, without clipping the knowledge learned from previous frames, the model is not appropriate to be used on subsequent frames.

5 Conclusion

In this paper, we proposed a solution for online VAD where offline training is no longer required. Our solution is based on a pixel-level MLP to reconstruct frames from pixel coordinates and DWT coefficients. Based on the information shifts between adjacent frames, an incremental learner is used to optimize the MLP online to produce detection results along a video stream. Our solution accurately detects anomalous events at the pixel-level, achieves strong performance on benchmark datasets, and surpasses other online VAD models by being capable to work with any number of abnormal frames in a video. Our future work focuses on improving performance by reducing the number of false positive detections.

¹⁴ Index numbers in the figure are 610 and 616, respectively, since our model begins analyzing this sequence at the 16_{th} frame.

References

1. Abati, D., Porrello, A., Calderara, S., Cucchiara, R.: Latent space autoregression for novelty detection. In: CVPR. pp. 481–490 (2019) [3](#)
2. Cai, R., Zhang, H., Liu, W., Gao, S., Hao, Z.: Appearance-motion memory consistency network for video anomaly detection. AAAI **35**(2), 938–946 (2021) [3](#), [11](#)
3. Chang, Y., Tu, Z., Xie, W., Yuan, J.: Clustering driven deep autoencoder for video anomaly detection. In: ECCV. pp. 329–345 (2020) [3](#), [11](#)
4. Doshi, K., Yilmaz, Y.: Continual learning for anomaly detection in surveillance videos. In: CVPRW. pp. 1025–1034 (2020) [4](#)
5. Doshi, K., Yilmaz, Y.: A modular and unified framework for detecting and localizing video anomalies. In: WACV. pp. 3982–3991 (2022) [4](#)
6. Doshi, K., Yilmaz, Y.: Rethinking video anomaly detection - a continual learning approach. In: WACV. pp. 3961–3970 (2022) [4](#)
7. Feng, J.C., Hong, F.T., Zheng, W.S.: Mist: Multiple instance self-training framework for video anomaly detection. In: CVPR. pp. 14009–14018 (2021) [3](#)
8. Finn, C., Abbeel, P., Levine, S.: Model-agnostic meta-learning for fast adaptation of deep networks. In: ICML. pp. 1126–1135 (2017) [4](#)
9. Georgescu, M.I., Barbalau, A., Ionescu, R.T., Khan, F.S., Popescu, M., Shah, M.: Anomaly detection in video via self-supervised and multi-task learning. In: CVPR. pp. 12742–12752 (2021) [2](#), [10](#), [11](#)
10. Giorno, A.D., Bagnell, J.A., Hebert, M.: A discriminative framework for anomaly detection in large videos. In: ECCV. pp. 334–349 (2016) [1](#), [2](#), [4](#), [11](#)
11. Gong, D., Liu, L., Le, V., Saha, B., Mansour, M.R., Venkatesh, S., Hengel, A.v.d.: Memorizing normality to detect anomaly: Memory-augmented deep autoencoder for unsupervised anomaly detection. In: ICCV. pp. 1705–1714 (2019) [3](#)
12. Hasan, M., Choi, J., Neumann, J., Roy-Chowdhury, A.K., Davis, L.S.: Learning temporal regularity in video sequences. In: CVPR. pp. 733–742 (2016) [3](#)
13. Hinami, R., Mei, T., Satoh, S.: Joint detection and recounting of abnormal events by learning deep generic knowledge. In: ICCV. pp. 3639–3647 (2017) [3](#)
14. Ionescu, R.T., Khan, F.S., Georgescu, M., Shao, L.: Object-centric auto-encoders and dummy anomalies for abnormal event detection in video. In: CVPR. pp. 7834–7843 (2019) [3](#)
15. Ionescu, R.T., Smeureanu, S., Alexe, B., Popescu, M.: Unmasking the abnormal events in video. In: ICCV. pp. 2914–2922 (2017) [1](#), [2](#), [4](#), [11](#)
16. Jin, B., Hu, Y., Tang, Q., Niu, J., Shi, Z., Han, Y., Li, X.: Exploring spatial-temporal multi-frequency analysis for high-fidelity and temporal-consistency video prediction. In: CVPR. pp. 4553–4562 (2020) [5](#)
17. Kingma, D.P., Ba, J.: Adam: A method for stochastic optimization. In: ICLR (2015) [10](#)
18. Liu, W., Luo, W., Li, Z., Zhao, P., Gao, S.: Margin learning embedded prediction for video anomaly detection with a few anomalies. In: IJCAI. pp. 3023–3030 (2019) [3](#)
19. Liu, W., Luo, W., Lian, D., Gao, S.: Future frame prediction for anomaly detection - a new baseline. In: CVPR. pp. 6536–6545 (2018) [3](#)
20. Liu, Y., Li, C., Póczos, B.: Classifier two sample test for video anomaly detections. In: BMVC. p. 71 (2018) [1](#), [2](#), [4](#), [10](#), [11](#)
21. Liu, Z., Nie, Y., Long, C., Zhang, Q., Li, G.: A hybrid video anomaly detection framework via memory-augmented flow reconstruction and flow-guided frame prediction. In: ICCV. pp. 13588–13597 (2021) [3](#), [11](#)

22. Lu, C., Shi, J., Jia, J.: Abnormal event detection at 150 fps in matlab. In: ICCV. pp. 2720–2727 (2013) [9](#)
23. Lu, Y., Yu, F., Reddy, M.K.K., Wang, Y.: Few-shot scene-adaptive anomaly detection. In: ECCV. pp. 125–141 (2020) [4](#), [11](#)
24. Luo, W., Liu, W., Gao, S.: A revisit of sparse coding based anomaly detection in stacked rnn framework. In: ICCV. pp. 341–349 (2017) [3](#), [10](#)
25. Lv, H., Chen, C., Cui, Z., Xu, C., Li, Y., Yang, J.: Learning normal dynamics in videos with meta prototype network. In: CVPR. pp. 15425–15434 (2021) [4](#), [11](#)
26. Mahadevan, V., Li, W., Bhalodia, V., Vasconcelos, N.: Anomaly detection in crowded scenes. In: CVPR. pp. 1975–1981 (2010) [9](#)
27. Markovitz, A., Sharir, G., Friedman, I., Zelnik-Manor, L., Avidan, S.: Graph embedded pose clustering for anomaly detection. In: CVPR. pp. 10536–10544 (2020) [3](#)
28. Mohammadi, B., Fathy, M., Sabokrou, M.: Image/video deep anomaly detection: A survey (2021) [2](#), [4](#)
29. Morais, R., Le, V., Tran, T., Saha, B., Mansour, M., Venkatesh, S.: Learning regularity in skeleton trajectories for anomaly detection in videos. In: CVPR. pp. 11988–11996 (2019) [3](#)
30. Nguyen, T.N., Meunier, J.: Anomaly detection in video sequence with appearance-motion correspondence. In: ICCV. pp. 1273–1283 (2019) [3](#)
31. Nichol, A., Achiam, J., Schulman, J.: On first-order meta-learning algorithms (2018) [8](#)
32. Ouyang, Y., Sanchez, V.: Video anomaly detection by estimating likelihood of representations. In: ICPR. pp. 8984–8991 (2021) [3](#)
33. Pang, G., Yan, C., Shen, C., Hengel, A.v.d., Bai, X.: Self-trained deep ordinal regression for end-to-end video anomaly detection. In: CVPR. pp. 12170–12179 (2020) [4](#)
34. Park, H., Noh, J., Ham, B.: Learning memory-guided normality for anomaly detection. In: CVPR. pp. 14360–14369 (2020) [3](#)
35. Purwanto, D., Chen, Y.T., Fang, W.H.: Dance with self-attention: A new look of conditional random fields on anomaly detection in videos. In: ICCV. pp. 173–183 (2021) [2](#), [3](#)
36. Ramachandra, B., Jones, M.J., Vatsavai, R.R.: A survey of single-scene video anomaly detection (2020) [2](#), [4](#)
37. Ravanbakhsh, M., Nabi, M., Sangineto, E., Marcenaro, L., Regazzoni, C., Sebe, N.: Abnormal event detection in videos using generative adversarial nets. In: ICIP. pp. 1577–1581 (2017) [3](#)
38. Shen, G., Ouyang, Y., Sanchez, V.: Video anomaly detection via prediction network with enhanced spatio-temporal memory exchange. In: ICASSP. pp. 3728–3732 (2022) [3](#)
39. Sitzmann, V., Martel, J.N., Bergman, A.W., Lindell, D.B., Wetzstein, G.: Implicit neural representations with periodic activation functions. In: NeurIPS (2020) [6](#), [10](#)
40. Sultani, W., Chen, C., Shah, M.: Real-world anomaly detection in surveillance videos. In: CVPR. pp. 6479–6488 (2018) [3](#)
41. Sun, C., Jia, Y., Hu, Y., Wu, Y.: Scene-aware context reasoning for unsupervised abnormal event detection in videos. In: ACM MM. p. 184–192 (2020) [3](#), [11](#)
42. Tancik, M., Mildenhall, B., Wang, T., Schmidt, D., Srinivasan, P.P., Barron, J.T., Ng, R.: Learned initializations for optimizing coordinate-based neural representations. In: CVPR. pp. 2846–2855 (2021) [6](#)

43. Tancik, M., Srinivasan, P.P., Mildenhall, B., Fridovich-Keil, S., Raghavan, N., Singhal, U., Ramamoorthi, R., Barron, J.T., Ng, R.: Fourier features let networks learn high frequency functions in low dimensional domains. In: *NeurIPS* (2020) **6**
44. Tian, Y., Pang, G., Chen, Y., Singh, R., Verjans, J.W., Carneiro, G.: Weakly-supervised video anomaly detection with robust temporal feature magnitude learning. In: *ICCV*. pp. 4975–4986 (2021) **3**
45. Vu, H., Nguyen, T.D., Le, T., Luo, W., Phung, D.: Robust anomaly detection in videos using multilevel representations. *AAAI* **33**(01), 5216–5223 (2019) **3**
46. Wang, S., Zeng, Y., Liu, Q., Zhu, C., Zhu, E., Yin, J.: Detecting abnormality without knowing normality: A two-stage approach for unsupervised video abnormal event detection. In: *ACM MM*. p. 636–644 (2018) **4**
47. Wang, Z., Zou, Y., Zhang, Z.: Cluster attention contrast for video anomaly detection. In: *ACM MM*. p. 2463–2471 (2020) **11**
48. Xu, D., Ricci, E., Yan, Y., Song, J., Sebe, N.: Learning deep representations of appearance and motion for anomalous event detection. In: *BMVC*. pp. 8.1–8.12 (2015) **3**
49. Ye, M., Peng, X., Gan, W., Wu, W., Qiao, Y.: Anopcn: Video anomaly detection via deep predictive coding network. In: *ACM MM*. p. 1805–1813 (2019) **3**
50. Zaheer, M.Z., Mahmood, A., Astrid, M., Lee, S.I.: Claws: Clustering assisted weakly supervised learning with normalcy suppression for anomalous event detection. In: *ECCV*. pp. 358–376 (2020) **3**
51. Zaigham Zaheer, M., Lee, J.H., Astrid, M., Lee, S.I.: Old is gold: Redefining the adversarially learned one-class classifier training paradigm. In: *CVPR*. pp. 14171–14181 (2020) **3**
52. Zhao, Y., Deng, B., Shen, C., Liu, Y., Lu, H., Hua, X.S.: Spatio-temporal autoencoder for video anomaly detection. In: *ACM MM*. p. 1933–1941 (2017) **3**
53. Zhong, J.X., Li, N., Kong, W., Liu, S., Li, T.H., Li, G.: Graph convolutional label noise cleaner: Train a plug-and-play action classifier for anomaly detection. In: *CVPR*. pp. 1237–1246 (2019) **3**
54. Zhu, Y., Newsam, S.D.: Motion-aware feature for improved video anomaly detection. In: *BMVC*. p. 270 (2019) **3**